NUMERICAL STUDY ON HEAT TRANSFER IN A TUBE WITH CONICAL-MESH FRUSTUMS INSERTED

Zhen Cao[a], Huibao Luan[a, b], Zan Wu[a], Bengt Sunden[a, *]
*Author for correspondence
a. Department of Energy Sciences, Lund Unveristy, Lund SE-22100, Sweden
b. Research and Development Division, Shenhua Ningxia Coal Industry Group Co. Ltd, China

E-mail: Bengt.Sunden@energy.lth.se

ABSTRACT

In this work, an innovative enhanced heat transfer tube (EHTT) is proposed, inserted with segmented conical-mesh frustums. The diameter of the bottom surface and the pitch between conical frustums were investigated while the diameter of the tube and apex angle are fixed at 20 mm and 60°, respectively. The ratio between the height of the frustum and that of the sliced part was set as a golden ratio (1.618), which is regarded as the optimal in nature. Numerical simulations were employed to study the performance of the enhanced heat transfer tube in the laminar flow region and the effects of the parameters on performance were compared. To save the workload and time of simulation, the equal equivalent diameter and total flow area criteria were adopted to simplify the 3-Dimensional mesh pores to 2-Dimensional mesh pores. Besides a multiscale grid system was built to link the micron scale of the mesh pores and macroscale of the tube and periodic boundary conditions were used. The results demonstrated that the flow and temperature fields were modeled effectively, with larger velocity and velocity gradient in the vicinity of the wall as well as smaller velocity in the bulk flow region, which produced better performance of heat transfer with a relatively low friction penalty. The EHTT could obtain 3.3 times higher performance than bare tube, based on the cases studied. It was also shown that Nusselt number increased as the Reynolds number increased, and the EHTT performed better with a larger bottom diameter and smaller pitch of the conical frustums. Surprisingly, for the frustums in which the ratio between the bottom diameter and tube diameter was 0.8, it was indicated that the Nusselt number increased significantly with a slight friction decrease when the ratio between the pitch and tube diameter decreased from 3 to 2.5. This study provides a new insight into heat transfer enhancement and tube configuration, which has a wide engineering application potential.

1. INTRODUCTION

Heat exchangers are widely used in many energy conversion and power generation systems. There is an urgent need to develop high-efficient heat transfer technology for energy saving and environmental protection. In the past few decades, many enhanced heat transfer technologies have been developed, including active and passive methods [1]. Passive methods are more accepted because they do not need external power. Among them, artificial roughness has been extensively studied because of its high thermal-hydraulic performance. Wang and Sunden [2] experimentally studied flow and heat transfer in a rectangular duct roughened by broken V-shaped ribs. Han et al. [3] investigated the effects of rib configurations on the performance in ribbed rectangular channels. Moon et al. [4] evaluated the performance of various rib shapes in rectangular channels. Zheng et al. [5] conducted a numerical study on the flow and heat transfer in a circular tube with inclined ribs. In addition, dimple and groove shaped roughnesses have also been studied [6-7]. The performances of tubes with different inserts, such as twisted tape, wire coil, conical strip, conical ring and mesh-conical insert were also widely investigated. The performance of twisted tapes for different lengths and widths were studied in [8-9], and the twisted tape combined with ribs and winglet was also reported in Refs. [10]. Yakut and Sahin [11] experimentally studied the performance of a tube inserted with a wire coil in laminar flow, transition flow and turbulent region. Cao and Xu [12] studied the flow and heat transfer in a tube inserted with mesh cones. Wang and Sunden [13] compared the performance of a tube with twisted tapes and wire coil, and it was shown that the thermal-hydraulic performance of inserts was better in the laminar flow region. As the aforementioned, the artificial roughness techniques do not work effectively in the laminar regime where the thermal resistance is not limited to a thin boundary layer adjacent to the flow. Instead, insert devices that mix the bulk flow are suitably employed for heat transfer enhancement in laminar flow regime.

NOMENCLATURE

C_p	[J/(kg K)]	Specific heat
Nu_b	[-]	Nusselt number for the bare tube, 4.36
p	[Pa]	Pressure
q	[W/m^2]	Heat flux
T	[K]	Temperature
y	[m]	The first fluid layer thickness near the wall
Special characters		
λ	[W/(m K)]	Thermal conductivity
μ	[Pa S]	Dynamic viscosity
ρ	[kg/m^3]	Density
Subscripts		
ave		Average
f		Fluid
in		Inlet
w		Wall

Here we proposed an innovative enhanced heat transfer tube (EHTT) with the conical-mesh frustums inserted, which has never been reported in the open literature. Compared with the conical-ring insert in Ref. [14], the conical-mesh-frustum insert

may reduce the flow friction effectively due to the porous structure. Computational fluid dynamics technology (CFD) combined with periodic boundary conditions was employed to investigate the performance of the tube. The paper is organized as follows: section 2 describes the EHTT structure and 3D to 2D conversion of the mesh pores; section 3 introduces the numerical simulation strategy; section 4 reports the results and discussions for the new findings, in which section 4.1 presents the validation of simulation strategy, section 4.2 provides the thermal-hydraulic performance of the EHTT and the new findings, and section 4.3 gives the explanations on the new findings.

2. THE ENHANCED HEAT TRANSFER TUBE (EHTT)

The EHTT was constructed by inserting segmented conical-mesh frustums into the heat transfer tube (see Fig. 1(a)). These were supposed to modulate the flow and temperature fields to enhance the heat transfer. A 2D coordination system was built with r as the radial coordinate and x as the axial flow coordinate as shown in Fig. 1(a), where several parameters were labelled as below: the diameter of the tube D, the length of the bare tube section L_1, the length of the tube with inserts L_2, the apex angle of the insert α, the diameter of the bottom of the insert δ and the pitch between the inserts S. In this study, the parameters were set as D = 20.0 mm, L_1 = 200.0 mm, L_2 = 1000.0 mm, δ/D = 0.6, 0.7 and 0.8, S/D = 2, 2.5 and 3 and α = 60°. In addition, the ratio between the height of the frustum and that of the sliced cone was set as a golden ratio (1.618), because it is regarded as the optimal in nature.

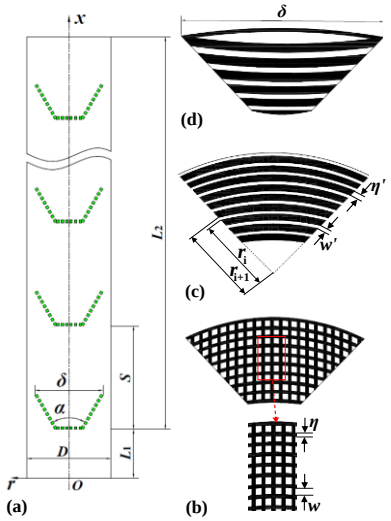

Figure 1 The proposed EHTT and 3D to 2D conversion of the mesh screen.

The conical-mesh frustum has porous surfaces with ten thousands of pores, which results in large challenges on the geometry building and grid generation. For example, in a domain defined above (D = 20.0 mm, L_1 = 200.0 mm, L_2 = 1000.0 mm, δ/D = 0.6, S/D = 2), there are 13369 mesh pores and nearly 200 million grid points for the mesh of *PPI* (pores per inch) = 80, which is nearly infeasible for the current computational resources. Therefore, two methods were proposed to decrease the computational demands, one is the dimensional conversion and the other is the periodic boundary condition. The conversion from 3D to 2D is described here and the periodic boundary condition will be introduced latter. Figure 1(b) shows a fan-shaped mesh screen which is fabricated as a conical-mesh frustum, where the width of the mesh pore w = 0.194 mm and the thickness of the mesh wire η = 0.130 mm, respectively (*PPI* = 80). According to the conversion method introduced in Ref. [13], the three-dimensional mesh screen (Fig. 1(b)) can be simplified as a two-dimensional one (Fig. 1(c)) with equivalent width of the mesh pore w' and thickness of the mesh wire η' following the equivalent mesh pore width criterion and the equivalent mesh pore area criterion, where $w' = 0.5w$ and $\eta' = \eta + \eta^2/2w$

As stated above, the dimensions of the 2D mesh screen used in the present study are as follows: w' = 0.087 mm and η' = 0.173 mm. The stripe mesh screen was created after the 3D to 2D conversion, and winding the stripe mesh screen forms the simplified conical-mesh frustum (Fig. 1(d)) which is coincident with the 2D simulation.

3. THE NUMERICAL SIMULATION AND METHOD

3.1 Governing equations and boundary conditions

In this study, the effects of δ and S on the laminar flow and heat transfer with water as the working fluid were numerically investigated, with δ/D = 0.6, 0.7 and 0.8, S/D = 2, 2.5 and 3. Normally, the transition from laminar Poiseuille flow to turbulent flow in a circular tube is generally understood to have a minimum lower critical Reynolds number between 1800 and 2300 [15], but the inserts will promote the laminar-turbulent transition [7]. Thus the Reynolds numbers involved in this study ranged from 100 to 1000. Several assumptions were made as shown below:

- Steady and fully developed flow and heat transfer
- Rigid mesh screen without vibration during the flow and heat transfer processes
- Incompressible Newtonian fluid with constant physical properties
- Negligible the effects of gravity and viscous heating as well as the heat conduction within the mesh wires

A 2D steady incompressible flow and heat transfer model was used for the present simulation. The governing equations in a Cartesian coordinate system are as below:

$$\nabla\cdot\left(\rho\vec{U}\right)=0 \tag{1}$$

$$\nabla\cdot\left(\rho\vec{U}\vec{U}\right)=-\nabla p+\nabla\cdot\left[\mu\left(\nabla\vec{U}\right)\right] \tag{2}$$

$$\nabla\cdot\left(\rho C_{\mathrm{p}}T\vec{U}\right)=\nabla\cdot\left(\lambda\nabla T\right) \tag{3}$$

Figure 2(a) shows half of the computational domain due to the symmetrical behaviour of the tube, along with a periodic unit shown in Fig. 2(b). A parabolic velocity distribution was implied on the entrance of the tube:

$$u_{\mathrm{in}}=2u_{\mathrm{ave}}\left[1-\left(2r/D\right)^2\right] \tag{4}$$

where u_{ave} is the inlet average velocity. The Reynolds number was defined as

$$Re=\rho D u_{\mathrm{ave}}/\mu \tag{5}$$

The boundary conditions (BCs) implied on the computational domain (Fig. 2(a)) were summarized here:

- Inlet BC at $x = 0$: $u = u_{in}$ given by Eqs.(4) and (5), $v = 0$, $T = 293.15$ K;
- Outlet BC at $x = L_1+L_2$: $p = 1.013\times10^5$Pa;
- Wall BC at $r = 0.5D$: $u = v = 0$， $q = q_w = \pi\cdot D\cdot L / m\cdot C_p\cdot\Delta T$ ($\Delta T = 10$K was assumed in this study);
- Symmetric BC at r=0: v=0, $\partial T / \partial r = \partial u / \partial r = 0$

Because of the periodic feature of EHTT, periodic boundary condition with the given mass flow rate ($m = \rho\cdot u_{ave}\cdot\pi\cdot D^2/4$) can be employed to study the fully developed flow and heat transfer. The detailed introduction on periodic BC can be found in Ref. [16].

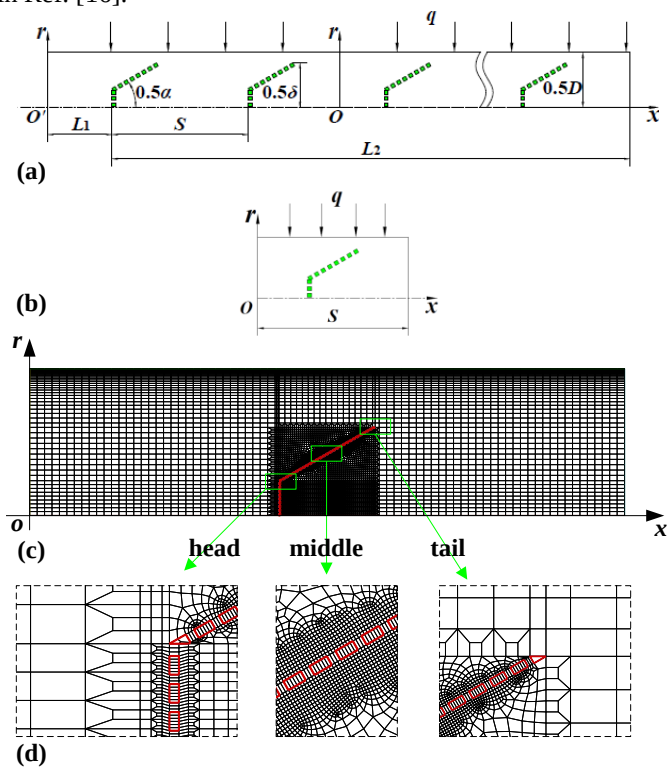

Figure 2 The computational domain and grid system: (a) full length domain, (b) periodic domain, (c) grid system, (d) locally enlarged grids at three positions

3.2 Grid generation and solution strategy

This study used the multiscale grid generation technique, which is similar to that in Ref. [12]. The periodic boundary condition required exactly the same grids on the two periodic planes which were linked together in GAMBIT 2.2.3. Figure 2(c) shows the grid system for the periodic unit. Fig. 2(d) indicates the details of the grid system at three positons, i.e., head, middle and tail of the frustum, respectively. The divided block grid generation method was applied to improve the grid quality, where the computational domain could be divided into three blocks: i the block upstream of the head, ii the block wrapping the frustum and iii the block downstream of the tail.

- In the blocks i and iii, uniformly structured grids were generated with 0.5 mm size in the flow direction, and the grids in the vicinity of the wall were extremely fine.
- In the block ii, the grid generation was a little complicated, w was further divided into two parts: the upper triangular region and the lower rectangular region. The quad-pave grid generation method was employed in the upper triangular region which made the grid coarser and coarser from the mesh pores to the boundary of the region (Fig. 2(d) middle) while the quad-map grid generation method was employed in the lower rectangle region. To bridge the grids system of the three blocks; the 4:2 grid transition method was applied to make it (Fig. 2(d) head and tail).

It was found that the flow and heat transfer were sensitive to the grid number in the mesh pores, so a grid independence test was carried out and the results are shown in table 1. Four sets of grid system; case1, case2, case3 and case4 for one, two, three and four grids in mesh pores, respectively; were tested in terms of *Nu* at *Re* = 100. It was found that the deviation of *Nu* between case3 and case4 was only 0.034%, showing that the grid system with three grids in mesh pores was adequately dense for the simulations. Accordingly, this grid system was adopted in the subsequent simulations reflecting a compromise between computational time and accuracy.

The SIMPLE algorithm was used to solve the governing equations with a second-order upwind discretization scheme for momentum and energy equations based on the commercial code Fluent16. The simulations were performed on a HP workstation, which has 8-core CPUs (3.5GHz each) and 16 GB of RAM. It took about 0.5 h for each case.

Table 1 Grid independence test

Grid case	Grid number	*Nu*	$Error_{Nu}$
case1	7974	6.788481	0.269%
case2	9345	6.799429	0.108%
case3	**12012**	**6.804461**	**0.034%**
case4	19141	6.806775	baseline

3.3 The general flow and heat transfer characteristics

The flow and heat transfer characteristics need to be analyzed after numerical convergence has been achieved. The wall heat flux passed through the grid closest to the wall by heat conduction because the no slip wall condition. The thickness of the grid is set as $y = 2.5\times10^{-7}$ m, which is validated to be sufficiently thin to capture the boundary layer characteristics. Assuming the temperature of the grid as T_{grid}, the wall temperature T_w is computed according to the Fourier thermal conduction law:

$$T_w = \frac{qy}{\lambda} + T_{grid} \tag{6}$$

The local Nusselt number is given by:

$$Nu_x = \frac{q}{T_w - T_f}\times\frac{D}{\lambda} \tag{7}$$

where the fluid temperature T_f is defined as:

$$T_f = \int \rho C_p u T dA / \int \rho C_p u dA \tag{8}$$

The overall Nusselt number is calculated as:

$$Nu = \frac{q}{T_{w,ave} - T_{f,ave}}\times\frac{D}{\lambda} \tag{9}$$

where $T_{w,ave}$ is the average wall temperature, $T_{f,ave}$ is the average fluid temperature.

The Darcy friction factor is given by:

$$f = (\Delta p / S) \times D / (\rho u_{ave}^2 / 2) \quad (10)$$

4. RESULT AND DISCUSSION

4.1 Validation of the numerical simulation

The validation work in the present study was separated into two steps, the first for the periodic boundary condition validation and the other for the solution strategy. Figure 3(a) shows the local *Nu* distribution along the flow direction both for full-length and periodic computations at *Re* = 100. For the full-length domain, the *Nu* at the entrance region is considerably high because of the entrance effect, and then it decreases sharply. Meanwhile the *Nu* performs in a periodic behavior after twelve periodic units, which imply that the flow and heat transfer are fully developed [16]. Furthermore, the *Nu* of the periodic domain agrees exactly with that of the fully developed full-length domain so that it is reasonable and accurate to employ the periodic boundary condition to study the fully developed flow and heat transfer. Afterwards, the validation for the solution strategy was done by comparing the computed results with those in Ref [17], as shown in Fig. 3(b). Reference [17] studied laminar periodic flow and heat transfer in a 2D horizontal channel with staggered diamond-shaped baffles under constant wall temperature. The compared case was taken from Fig. 6 in Ref. [17] for a flat baffle. The results show the deviation of -4.4% - 1.7% so that the simulation strategy employed in this study is reliable.

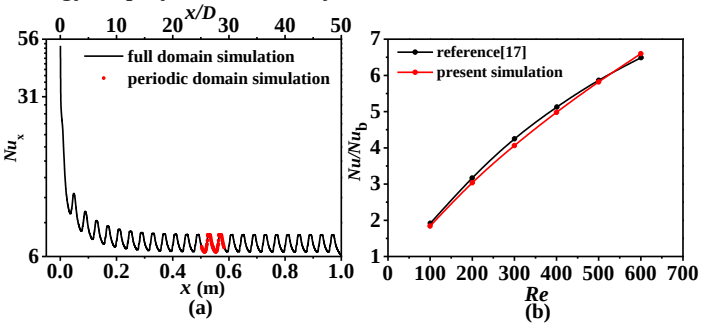

Figure 3 Validation of the present simulation: (a) the validation for periodic boundary condition, (b) the validation for the solution strategy, compared with Ref. [17]

4.2 The thermal-hydraulic behavior for the EHTT

The performances of the EHTT with different *δ/D* and *S/D* were evaluated by the overall Nusselt number *Nu* and the friction factor *f*, shown in Fig. 4. It is indicated that the *Nu* are all significantly larger than 4.36 for a bare tube regardless of *δ/D* and *S/D* and the *Nu* of the tube with smaller *S/D* is much higher. The *Nu* increases as *Re* is increased but the trends are a little different. For the tube with *δ/D* = 0.6 (Fig. 4(a)), the increase of *Nu* versus *Re* tends to be more and more gentle when *Re* < 500, but afterwards it is found to be significant. A nearly similar trend is almost valid for the tube with *δ/D* = 0.7, except that the increase is almost linear when *Re* < 500, and later the increase is much more rapid (Fig. 4(b)). However, the trend is rather different for the tube with *δ/D* = 0.8 (Fig. 4(b)), where the *Nu* increases significantly before *Re* = 500 and then the increase becomes more gentle. Therefore, *Re* = 500 is regarded as a knee point where $\frac{\partial^2 Nu}{\partial Re^2} = 0$. By comparing the three subfigures in Fig. 4, the *Nu* of the tube with larger *δ/D* is much higher. For example, regarding the tube of *S/D* = 2, *Nu* = 7.79 for *δ/D* = 0.6, *Nu* = 9.26 for *δ/D* = 0.7 and *Nu* = 13.40 for *δ/D* = 0.8 at *Re* = 500. The *Nu* covers the range of 6.06 - 14.21, which is 1.4-3.3 times higher than that for the bare tube.

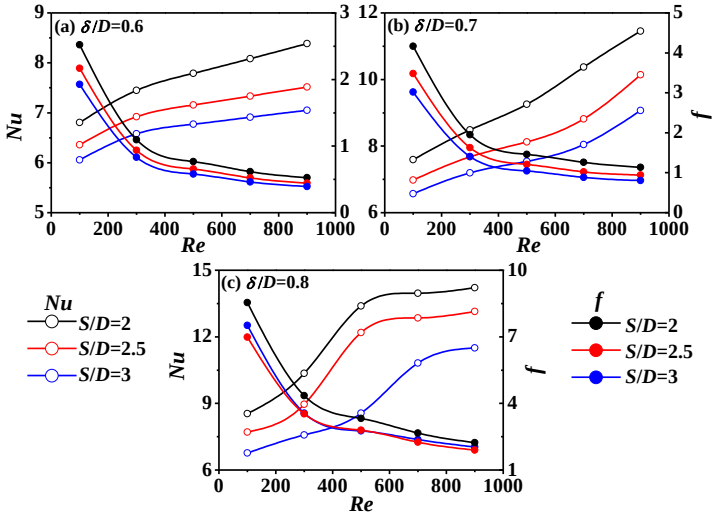

Figure 4 The Nusselt number and friction factor for EHTT

The friction factor *f* represents the pressure drop. It is found that *f* decreases with increasing *Re*. For each subfigure in Fig. 4, the slopes of *f* versus *Re* are sharp at low *Re*, and then become gentle beyond the transitional Reynolds number in a narrow range of 300 - 400. It is worth noting that for the EHTT of *δ/D* = 0.8, *f* is decreased when *S/D* changes from 3 to 2.5, indicating higher heat transfer is performed with less pressure drop penalty.

As stated above, three main findings in this study can be summarized:

- The *Nu* increases as *Re* increases, with different slopes below and beyond *Re* = 500.
- Larger *δ/D* induces higher *Nu* and better performance
- For the EHTT of *δ/D* = 0.8, *f* decreases when *S/D* changes from 3 to 2.5, which differs significantly from conventional cases.

4.3 Explanations for the new findings

4.3.1 Varied slopes of *Nu* against *Re* (the occurrence of knee point)

Section 4.2 described the trend of *Nu* versus *Re*. In this section, more explanations for the trend are given, with the cases of *δ/D* = 0.8 and *S/D* = 2 as examples. Figure 5 examines local *Nu* versus *x* and dimensionless *x/D* in a periodic unit at three runs, namely *Re* = 100, 500 and 900. It is apparent that the amplitude of increase from *Re* = 100 to 500 is much higher than that from *Re* = 500 to 900, which is thoroughly coincident with the trend observed in Fig. 4(c). Furthermore, the

distributions of the axial velocity normalized as u/u_{ave} and temperature normalized as $(T - T_{f,\,x=0.01}) / (T_w - T_{f,\,x=0.01})$ over the tube cross section x = 0.01, which is ahead of the conical-mesh frustum insert, were plotted in Fig. 6. The flow and temperature fields can also be imagined to some extent by referring to Fig. 6. In the laminar flow region, it works less for heat transfer as only the flow near the wall is promoted [8]. Instead the whole flow needs to be modulated. Figure 6(a) tells that the flow field is thoroughly different from that in the bare tube, with two peaks near the wall, which indicates a much larger velocity gradient near the wall and a thinner boundary layer. It is worth noting that the increase of the velocity gradient from *Re* = 100 to 500 is more intense than that from *Re* = 500 to 900. The temperature is strongly related to the velocity, Fig. 6(b) shows a more uniform temperature field for *Re* = 500 and 900. The thermal boundary layer thickness decreases greatly when *Re* increases from 100 to 500. However, it decreases gently when *Re* increases from 500 to 900. Therefore, the present flow and temperature distributions are beneficial to heat transfer enhancement, with varied scopes of *Nu* versus *Re*.

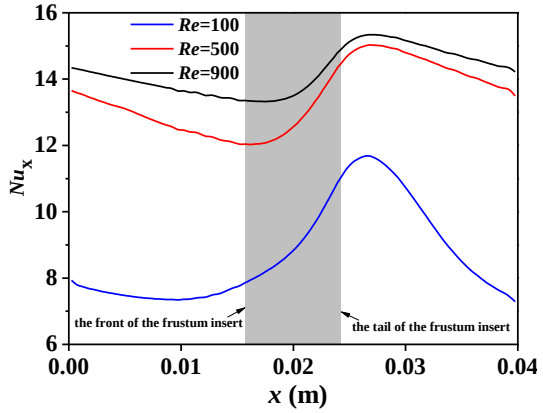

Figure 5 The local Nusselt number distribution along flow direction, with δ/D = 0.8 and S/D = 2.

4.3.2 The performance of the EHTT for different δ/D

As described above, the EHTT with smaller S/D and larger δ/D performs better. It is easy to understand why a smaller S/D is more advantageous than others, because a larger region is not modulated by the inserts if S/D becomes large. Here more attention will be paid to δ/D. Figure 7 demonstrates the flow and temperature fields for the EHTT for various δ/D. The different behaviours of flow and temperature fields explain the various performances of the EHTT.

When the fluid passes through the frustum, the pressure falls sharply because of throttle effect so that a recirculation region occurs (Fig. 7(a) Region 3). In Fig. 7(a), Region 1 is called the flow departure region and Region 2 is called the flow attachment region. It is Region 3 that takes the fluid away from the wall so that Region 2 appears and it is the gap between the tail tip of the insert and the wall that restricts the fluid flow so that it attaches to the wall and Region 1 is formed. Compared with Region 2, the velocity gradient near the wall is small and the wall temperature is high in Region 1, due to a thick thermal boundary layer. The flow and temperature fields in Region 2 are compressed strongly resulting in a larger velocity gradient and a thinner thermal boundary layer. Thus, Region 2 performs much better than Region 1. The mesh pores can balance the pressure to a different extent for different δ/D, so the flow field differs. Compared with Fig. 7(a), there is small Region1 and larger Region 2 in Fig. 7(b) and Region 1 almost disappears in Fig. 7(c). Thus, the EHTT with larger δ/D presents lower wall temperature and more uniform temperature field. Therefore, larger δ/D induces higher *Nu* and better heat transfer performance.

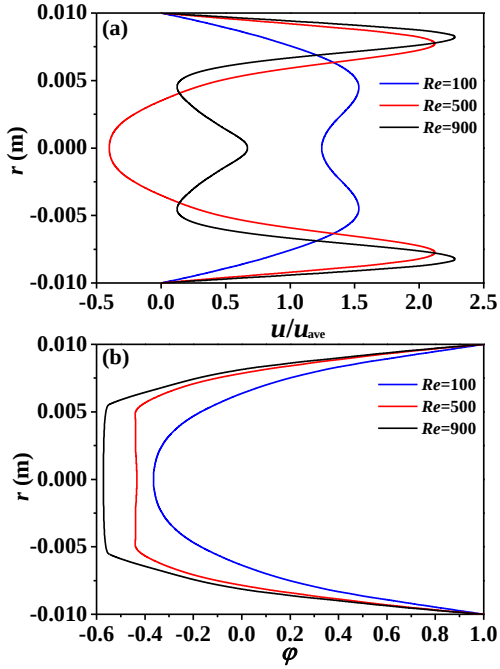

Figure 6 Effects of *Re* on axial velocity and temperature distribution over the tube cross section x = 0.01m, with δ/D = 0.8 and S/D = 2, where $\varphi = (T - T_{f,\,x=0.01}) / (T_w - T_{f,\,x=0.01})$.

4.3.3 The behavior of f for the EHTT with S/D = 2.5 and 3

It is surprising that f increases when S/D changes from 2.5 to 3 for the EHTT with δ/D = 0.8, which is distinctly different from conventional cases. Because the pressure is strongly coupled with velocity, it is essential to know how the flow fields behave. Figure 8 shows the velocity fields for these two cases at *Re* = 900. A recirculation region does not appear in the downstream region because of the balance of the pressure across the mesh screen by the mesh pores. However, the velocity fields in the upstream region are different in the two cases. In the case of S/D = 2.5 (Fig. 8(a)), the streamlines are straight-forward, indicating no recirculation there, whereas the streamlines behave differently, and recirculating flow appears right ahead of the mesh screen (marked as A in Fig. 8(b)), which induced the relatively higher pressure drop. This is the reason why the fraction is larger in the EHTT with S/D = 3 compared with S/D = 2.5 when δ/D = 0.8.

5. CONCLUSIONS

The thermal-hydraulic performances of EHTT inserted with conical-mesh frustums of different δ/D and S/D were numerically studied. It was found that the performances were

significantly better than the bare tube. The following conclusions can be drawn:

- For *Re* = 100-1000, the EHTT has *Nu* values which are 1.4 - 3.3 times of those in the bare tube.
- The EHTT with smaller *S/D* and larger *δ/D* performs better on heat transfer.
- *Re* = 500 is regarded as the knee point for the trends of *Nu* versus *Re*. The *Nu* behaves differently versus *Re* when *Re* < 500 and when *Re* > 500.
- As *Re* increases, the friction factor decreases sharply at low *Re* and then gently beyond *Re* = 300-400. Smaller *S/D* and larger *δ/D* induce higher friction. However, *f* decreases when *S/D* decreases from 3 to 2.5 for the EHTT of *δ/D* = 0.8.

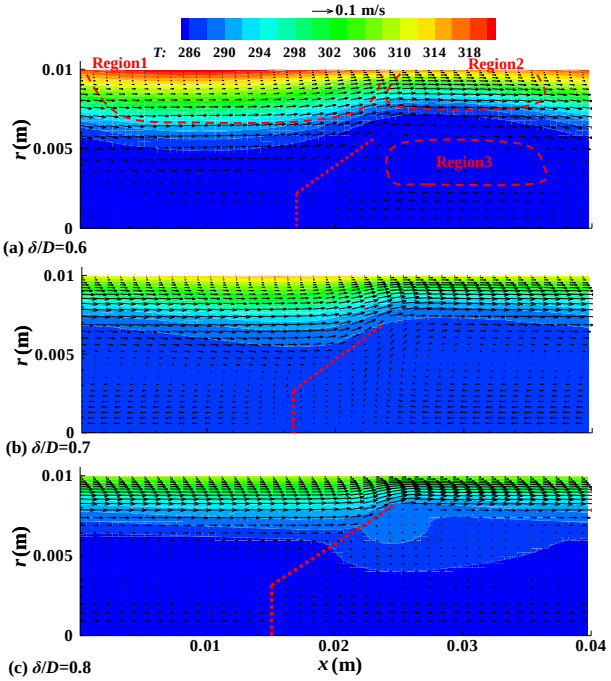

Figure 7 The flow and temperature fields for the EHTT with inserted conical-mesh frustums of *S/D* = 2 at *Re* = 900

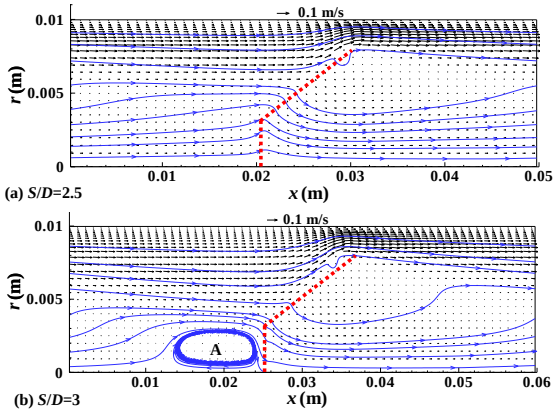

Figure 8 The flow fields for the EHTT inserted with conical-mesh frustums of *δ/D* = 0.8 at *Re* = 900

ACKNOWLEDGEMENT

The work is supported by the Swedish Research Council (VR) and China Scholarship Council (CSC).

REFERENCES

[1] Lin Z.H., Wang J., Li R.Y., and Cui G.M. Enhanced heat transfer technology, Chemical Industry Press, Beijing, 2006, pp. 5-6

[2] Wang L., and Sunden B., An experimental investigation of heat transfer and fluid flow in a rectangular duct with broken V-shaped ribs, *Experimental Heat Transfer*, Vol. 17, No. 4, 2004, pp. 243-259.

[3] Han J.C., Ou S., Park J.S., Lei C.K., Augmented heat transfer in rectangular channels of narrow aspect ratios with rib turbulators, *International Journal of Heat and Mass Transfer*, Vol. 32, No. 9, 1989, pp. 1619-1630.

[4] Moon M.A., Park M.J., and Kim K.Y., Evaluation of heat transfer performance of various rib shapes, *International Journal of Heat and Mass Transfer*, Vol. 71, 2014, pp. 275-284.

[5] Zheng N.B., Liu P., Shan F., Liu Z.C., and Liu W., Effect of rib arrangements on the flow pattern and heat transfer in an internally ribbed heat exchange tube, *International Journal of Heat and Mass Transfer*, Vol. 101, 2016, pp. 93-105.

[6] Zheng N.B., Liu P., Shan F Liu Z.C., and Liu W., Heat transfer enhancement in a novel internally grooved tube by generating longitudinal swirl flows with multi-vortexes, *Applied Thermal Engineering*, Vol. 95, 2016, pp. 421-432.

[7] Garcia A., Solano J.P., Vicente P.G., Viedma A., The influence of artificial roughness shape on heat transfer enhancement: Corrugated tubes, dimpled tube and wire coils, *Applied Thermal Engineering*, Vol. 35, 2012, pp. 196-201.

[8] Naga Sarada S., Sita Rama Raju A.V., Kalyani Radha K., and Shyam Sunder L., Enhancement of heat transfer using varying width twisted tape inserts, *International Journal of Engineering, Science and Technology*, Vol. 2, 2010, pp. 107–118.

[9] Eiamsa-ard S., Thianpong C., Eiamsa-ard P., and Promvonge P., Convective heat transfer in a circular tube with short-length twisted tape insert, *International Communications in Heat and Mass Transfer*, Vol. 36, 2009 pp. 365–371.

[10] Tanma S., Kaewkohkiat Y.Y., Skullong S., and Promvonge P., Heat transfer enhancement in tubular heat exchanger with double V-ribbed twisted-tapes, *Case Studies in Thermal Engineering*, Vol. 7, 2016, pp. 14-24.

[11] Yakut K., and Sahin B., The effects of vortex characteristics on performance of coiled wire turbulators used for heat transfer augmentation, *Applied Thermal Engineering*, Vol. 24, 2004, pp. 2427-2438.

[12] Cao Z., and Xu J.L., Modulated heat transfer tube with short conical-mesh inserts: A linking from microflow to macroflow, *International Journal of Heat and Mass Transfer*, Vol. 89, 2015, pp. 291-307.

[13] Wang L., and Sunden B., Performance comparison of some tube insets, *International Communication in Heat and Mass Transfer*, Vol. 29, No. 1, 2002, pp. 45-56.

[14] Promvonge P., Heat transfer behaviors in round tube with conical ring inserts, *Energy Conversion and Management*, Vol. 49, 2008, pp. 8-15.

[15] Sharp K.V., and Adrian R.J., Transition from laminar to turbulent flow in liquid filled microtubes, *Experiments in Fluids*, Vol. 36, 2004, pp. 741-747.

[16] Patankar S.V., Liu C.H., and Sparrow E.M., Fully developed flow and heat transfer in ducts having streamwise-periodic variations of cross-sectional area, *Journal of Heat Transfer*, Vol. 99, 1977, pp. 180-186.

[17] Sripattanapipat S., and Promvonge P., Numerical analysis of laminar heat transfer in a channel with diamond-shaped baffles, *International Communication in Heat and Mass Transfer*, Vol. 36 2009, pp. 32-38.